CHIN. PHYS. LETT. Vol. 38, No. 9 (2021) 098401

# Elastic Modulus, Hardness, and Fracture Toughness of $Li_{6.4}La_3Zr_{1.4}Ta_{0.6}O_{12}$ Solid Electrolyte

Shan Hu[1,2], Pengyu Xu[3], Luize Scalco de Vasconcelos[2], Lia Stanciu[3], Hongwei Ni[1*], and Kejie Zhao[2*]

[1]*State Key Laboratory of Refractories and Metallurgy, Wuhan University of Science and Technology, Wuhan 430081, China*
[2]*School of Mechanical Engineering, Purdue University, West Lafayette, Indiana 47907, USA*
[3]*School of Materials Engineering, Purdue University, West Lafayette, Indiana 47907, USA*

(Received 26 April 2021; accepted 17 August 2021; published online 2 September 2021)

$Li_{6.4}La_3Zr_{1.4}Ta_{0.6}O_{12}$ (LLZTO) is a promising inorganic solid electrolyte due to its high $Li^+$ conductivity and electrochemical stability for all-solid-state batteries. Mechanical characterization of LLZTO is limited by the synthesis of the condensed phase. Here we systematically measure the elastic modules, hardness, and fracture toughness of LLZTO polycrystalline pellets of different densities using the customized environmental nanoindentation. The LLZTO samples are sintered using the hot-pressing method with different amounts of $Li_2CO_3$ additives, resulting in the relative density of the pellets varying from 83% to 98% and the largest grain size of $13.21 \pm 5.22\,\mu m$. The mechanical properties show a monotonic increase as the sintered sample densifies, elastic modulus and hardness reach $158.47 \pm 10.10$ GPa and $11.27 \pm 1.38$ GPa, respectively, for LLZTO of 98% density. Similarly, fracture toughness increases from 0.44 to 1.51 $MPa{\cdot}m^{1/2}$, showing a transition from the intergranular to transgranular fracture behavior as the pellet density increases. The ionic conductivity reaches $4.54 \times 10^{-4}$ S/cm in the condensed LLZTO which enables a stable Li plating/stripping in a symmetric solid-state cell for over 100 cycles. This study puts forward a quantitative study of the mechanical behavior of LLZTO of different microstructures that is relevant to the mechanical stability and electrochemical performance of all-solid-state batteries.

DOI: 10.1088/0256-307X/38/9/098401

The ever-increasing demand of energy storage stimulates the development of high energy density, safer, and long cycle battery technologies.[1] The conventional Li-ion batteries using graphite and metal-oxide electrodes cannot meet the performance target of renewable energies and electrical vehicles.[2–4] Li metal has a specific capacity of 3860 mA·h/g and the lowest chemical potential, making it an ideal choice for the anode material. However, Li metal is not compatible with the widely used flammable liquid electrolytes, which limits its practical implementation in commercial use.[5–7] It is well known that Li metal is chemically unstable in the liquid electrolyte. The repetitive Li plating and stripping induce protuberance and sharp spikes, so-called dendrite, that tend to pass through the electrolyte and cause short circuits and even explosion of batteries.[8–11] The safety issue has become the most societal concern of the potential use of Li metal in electric vehicles. To enhance the energy density and to mitigate the safety risk, one possible solution is to introduce the solid-state electrolyte (SSE) to pair with the Li metal anode.[12,13] Among all the solid candidates, the garnet-type inorganic SSE, especially Ta doped $Li_7La_3Zr_2O_{12}$ (LLZTO), gains a wide attention because of the unparalleled advantages as follows: (1) a high ionic conductivity up to 1 mS/cm, (2) a good electrochemical stability with Li metal, and (3) a wide electrochemical-stable window (0.0–5.0 V).[14–17] However, the poor interfacial contact between the solid phases of Li and LLZTO becomes another raising problem which causes a large interfacial resistance and degradation of the electrochemical performance. Recent studies also show that Li transport through the defects likely form the dendrites within the solid electrolytes and the accumulated flaws eventually cause mechanical failure of batteries.[18,19] Realizing the promise of LLZTO in solid-state batteries is a pressing need and from this perspective, it is crucial to understand the mechanical properties of LLZTO and its compatibility and stability at the solid-solid interface.

Among the many notable studies, Shen *et al.* used synchrotron x-ray tomography to track the structural transformation in the $Li_7La_3Zr_2O_{12}$ (LLZO) electrolyte and showed that the mechanical failure occurred when the internal pores were interconnected.[20] Han *et al.* conducted first-principles computational modeling to confirm that the interfacial resistance arose because of the decomposition of the solid electrolyte.[21] Cheng *et al.* studied the mechanical behavior of $Li_{6.25}Al_{0.25}La_3Zr_2O_{12}$ and revealed Li transport through the polycrystalline

Supported by the National Science Foundation (Grant Nos. CMMI-1726392 and DMR-1832707) at Purdue University.
*Corresponding authors. Email: nihongwei@wust.edu.cn; kjzhao@purdue.edu
© 2021 Chinese Physical Society and IOP Publishing Ltd

solid electrolyte, which indicated Li deposition along the grain boundaries.[22] There have been many studies focusing on the improvement of the electrochemical performance of the LLZTO electrolyte, including coating the electrolyte onto the electrodes, infusing solid electrolyte into the separator, and foaming solid electrolyte in cell via *in situ* solidification, etc.[23–27] These strategies indeed provide effective solutions to boost the electrochemical merits, however, the mechanistic understanding particularly from the perspective of mechanical failure is still limited.[28] Understanding the relationship between the microstructure and the mechanical response of LLZTO is vital to decode the wholistic behavior of the solid-state batteries. The mechanical characterization of solid-state electrolytes in general remains a major challenge either because of the air sensitivity, such as the sulfide-based electrolytes, or the limited manufacturability of the condensed phase, such as the metal-oxide based electrolytes.[29] Therefore, there have been very few studies to date that systematically characterized the relationship between the mechanical properties of the solid electrolytes and their microstructures. This information is important for understanding the mechanical behavior of LLZTO, particularly at the interface with the Li metal during Li striping/plating cycles, which determines the capacity retention, mechanical stability, and electrochemical safety of all-solid-state batteries. Our goal here is to systematically measure the mechanical properties of LLZTO pellets of different grain structures so as to understand the relevant electrochemical performance.

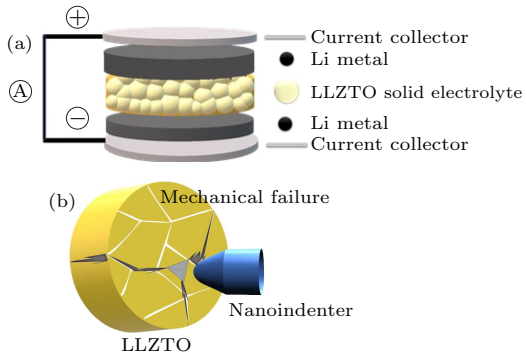


**Fig. 1.** Schematic illustrations of (a) a symmetric Li/LLZTO/Li battery cell containing the compacted polycrystalline LLZTO solid electrolyte, and (b) the mechanical characterization of the solid electrolyte pellet using nanoindentation.

We synthesize condensed LLZTO polycrystalline pellets using the hot-pressing method. LLZTO samples are sintered using different amounts of $Li_2CO_3$ additives, resulting in the density of the pellets varying from 83% to 98% and the largest grain size of $13.21 \pm 5.22\,\mu m$. Then, we employ the customized environmental nanoindentation, which is integrated in the Ar-filled glovebox, to measure the elastic modulus $E$, hardness $H$, and fracture toughness $K_c$ as schematically shown in Fig. 1(b). The mechanical properties of LLZTO show a monotonic increase with the increasing sintered sample density, elastic modulus and hardness reach $158.47 \pm 10.10$ GPa and $11.27 \pm 1.38$ GPa, respectively, for LLZTO of 98% relative density. Similarly, fracture toughness increases from $0.44\,MPa{\cdot}m^{1/2}$ to $1.51\,MPa{\cdot}m^{1/2}$, showing a transition from the intergranular to transgranular fracture behavior as the pellet density increases. Furthermore, we assemble the symmetric Li/LLZTO/Li cells [shown in Fig. 1(a)] to measure the ionic conductivity and to test the plating/stripping behavior over cycles. The ionic conductivity reaches $4.54 \times 10^{-4}$ S/cm in the condensed LLZTO which enables a stable Li shuttle for over 100 cycles. The results verify the relationship between the optimized mechanical properties of the solid electrolyte and the enhanced electrochemical performance of the solid-state cells.

*Experimental Methods.* The LLZTO composites were synthesized using the hot-pressing method with $Li_2CO_3$ as the Li salt additives. We took 0 wt%, 5 wt%, 10 wt%, and 20 wt% excess of $Li_2CO_3$ added into the as-received $Li_{6.4}La_3Zr_{1.4}Ta_{0.6}O_{12}$ powder, and yttria-stabilized zirconia milling was performed for 3 h. The mixed powders were hot-pressed into a disc of 11 mm diameter, and annealed at 1100 ℃ for 12 h with a heating rate of 5 ℃/min. After cooling, the samples were stored in the Ar-filled glovebox to avoid contamination. The LLZTO composites were examined via the archimedes method by measuring the weight and volume using ethanol as the immersion medium. The relative mass density of LLZTO pellets was determined to be 83%, 90%, 94% and 98%, respectively, with the excessive $Li_2CO_3$ of 0%, 20%, 10%, and 5%.

Next, the as-synthesized LLZTO samples were polished and sputtered with a Pt layer on both sides, which were used for the electrochemical impedance spectroscopy (EIS) test. The symmetric cells were assembled to test Li striping/plating and the cycling stability. Specifically, Li metal was placed on both sides of the polished LLZTO plate with the stainless steel and spring in the CR2032 type coin cell. The EIS test was performed using VersaSTAT3 (Princeton Applied Research) in the frequency range from 100 kHz to 0.1 Hz and an amplitude voltage of 5 mV. The cyclic performance was tested using a voltage window of 2.8 V to 4.2 V at a current density of $0.05\,mA/cm^2$ (BT-2043, Arbin). The ionic conductivity $\sigma$ is calculated from the equation

$$\sigma = \frac{1}{z} \cdot \frac{l}{s}, \tag{1}$$

where $z$ is the impedance, $l$ is the LLZTO plate thickness, and $s$ is the surface area.

X-ray diffraction (XRD, D8 Bruker x-ray diffractometer with Cu-Ka radiation) was used to charac-

terize the crystal structure of the LLZTO samples. The morphology and the chemical composition of the sample were examined using the scanning electron microscopy (SEM, FEI QUANTA 3D FEG) and the energy-dispersive x-ray spectroscopy (EDS). The TEM sample of the thickness around 100 nm was characterized by the FEI Talos 200X TEM system with the accelerate voltage of 200 kV.

Mechanical properties were measured by instrumented nanoindentation (G200 Nanoindenter, KLA) integrated in the glovebox to determine the elastic modulus, hardness, and fracture toughness at a constant strain rate of $0.05\,\mathrm{s}^{-1}$.[30] We give the hardness $H$, elastic modulus $E$, and $K_\mathrm{c}$ as follows:

$$H = \frac{P}{A_\mathrm{c}}, \tag{2}$$

$$\frac{1}{E_r} = \frac{1-v^2}{E} + \frac{1-v_\mathrm{i}^2}{E_\mathrm{i}}, \tag{3}$$

$$K_\mathrm{c} = \alpha\Big(\frac{E}{H}\Big)^{1/2}\Big(\frac{P}{c^{3/2}}\Big), \tag{4}$$

where $P$ is the load, $v$ and $\nu_\mathrm{i}$ are Poisson's ratio of the sample and the indenter, respectively; $E_\mathrm{i}$ is the elastic modulus of the indenter, and $E_r = 0.5S\sqrt{\pi/A_\mathrm{c}}$ with $S$ being the unloading slope of the load-displacement curve upon initial indenter removal. Poisson's ratio for the LLZTO sample and the indenter were assumed to be 0.26 and 0.07, respectively.[31–33] The area of contact $A_\mathrm{c}$ was calibrated using the standard fused silica sample. In Eq. (4), $c$ is the crack length, $P$ is the critical load that generates a crack of the length $c$, and $\alpha$ is an empirical constant. The effective crack length $c$ was calculated by the pop-in method which allowed to determine the crack length from the load-displacement curve. The indentation induced crack length follows the equation

$$c = \sqrt{2}h_\mathrm{m} + \Big(Q\frac{E'}{H} - \sqrt{2}\Big)h_x, \tag{5}$$

where $h_\mathrm{m}$ is the measured tip displacement, $h_x = h_\mathrm{m} - h_\mathrm{t}$ with $h_\mathrm{t}$ being the theoretical tip displacement, $Q$ is a material independent constant, and $E'$ and $H$ are the plane strain elastic modulus and hardness, respectively.

*Results and Discussions.* Figure 2 presents the XRD patterns of the LLZTO samples synthesized with different amounts of $Li_2CO_3$ additives. The excessive $Li_2CO_3$ plays an import role in the annealing process. The major diffraction peaks match well with PDF45-0109 ($Li_5La_3Nb_2O_{12}$), which is known as the cubic garnet phase.[34] Extra $La_2Zr_2O_7$ peaks exist when LLZTO is annealed with non-excessive $Li_2CO_3$, indicating the decomposition of LLZTO owing to the Li-deficient condition. On the other hand, it is observed from Fig. 2 that the crystallinity of LLZTO decreases with the excessive Li additives. Over 30% $Li_2CO_3$, the presence of the $LiAlO_2$ peaks demonstrates the interaction between the excessive $Li_2CO_3$ and the alumina crucible, which forms the $Li_2O$-$Al_2O_3$ compound.[35] Figure S1 in the Supplementary Material further shows the XRD patterns of LLZTO synthesized under various annealing temperatures. There is a mixture of the tetragonal phase, cubic garnets, and impurities of $La_2Zr_2O_7$ and $LiAlO_2$ at the sintering temperature of 900 ℃, suggesting that the tetragonal phase can easily react with the $Al_2O_3$ crucible. When the temperature increases up to 1000 ℃ and 1050 ℃, the $LiAlO_2$ phase disappears showing that the tetragonal phase is transferred to the cubic phase. When the sintering temperature reaches 1100 ℃, the LLZTO pellet is made of a pure cubic garnet phase without impurities.

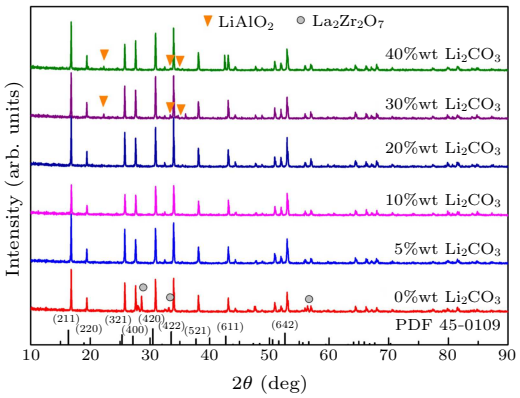


**Fig. 2.** XRD patterns of LLZTO pellets with different amounts of $Li_2CO_3$ additives.

Figures 3(a)–3(d) show the SEM images of the LLZTO composites annealed at 1100 ℃ for 12 h with different amounts of excessive $Li_2CO_3$. To explore the relation between the excessive $Li_2CO_3$ and the relative density of the pellets, the LLZTO samples are examined via the archimedes method by measuring the weight and volume using ethanol as the immersion medium. The relative densities of LLZTO polycrystalline samples are determined to be 83%, 90%, 94%, and 98%, respectively, with the excessive $Li_2CO_3$ of 0%, 20%, 10%, and 5% [Figs. 3(a)–3(d)]. At 0% $Li_2CO_3$ [Fig. 3(a)], the grains are mainly long-round or of an irregular shape with the average grain size of $2.79 \pm 0.65\,\mu\mathrm{m}$. Many throughout holes are observed in the sample. The grains are loosely compacted with visible boundaries, showing the sintering defects and high porosity in the LLZTO sample because of the Li-deficient condition. The intergranular morphology results in a lower relative density (∼83%), indicating that the Li salt is consumed to form the impurity phase ($La_2Zr_2O_7$) during the high temperature annealing, which is consistent with the XRD results. It is important to compensate the Li deficiency by adding the excessive Li salt. Figure 3(b) shows the microstructure of LLZTO annealed with 20% excessive $Li_2CO_3$. The grains are mostly round

and isolated with edges and a better contact, and the grain size increases up to $5.99 \pm 1.77\,\mu m$, suggesting a lower porosity and therefore an improved relative density (∼90%). However, according to the XRD results, when the $Li_2CO_3$ is over weighted, the excessive Li will react with the $Al_2O_3$ crucible. Figure 3(c) shows the SEM image of the LLZTO pellet when the amount of $Li_2CO_3$ decreases to 10%. The round and large grains with an average size of $8.93 \pm 2.56\,\mu m$ demonstrates a further improved packing density (∼94%). Figure 3(d) shows the image of the LLZTO sample (surface polished) with the optimized $Li_2CO_3$ of 5% and the inset shows the enlarged view (unpolished). The grains grow to the largest size of $13.21 \pm 5.22\,\mu m$ and are closely compacted to form an integrated morphology. The porosity is much reduced, and the relative density reaches ∼98%. Figure 3(e) shows the histograms of the grain size in LLZTO of different relative densities. It is clear that the grain grows larger with the increasing density of polycrystalline samples because of the optimized $Li_2CO_3$ additives. Overall, the microstructure of the LLZTO pellet transits from the intergranular to the transgranular feature with the increasing density, lower porosity, and less synthesized defects, which will benefit the interfacial contact and mechanical stability of the solid-state batteries.

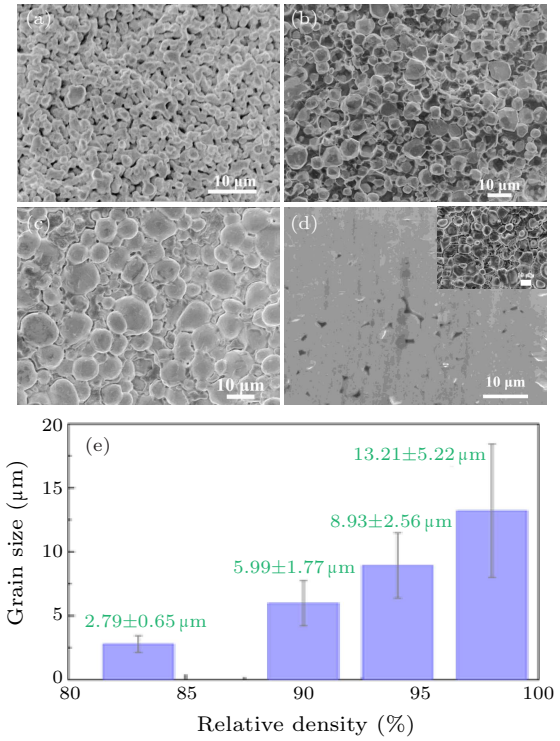


**Fig. 3.** SEM images of the sintered LLZTO pellets of different relative mass densities: (a) 83%, (b) 90%, (c) 94%, and (d) 98%. (e) The average grain size in the polycrystalline LLZTO of different densities.

We perform transmission electron microscopy (TEM) experiments to examine the crystallinity features of the LLZTO composites. The samples are prepared by the focus ion beam (FIB). Figure 4(a) shows the cross section of the LLZTO pellet of 98% relative density. A high-resolution TEM image in Fig. 4(b) shows the clear lattice fringe of the grains and the amorphous surface layer of the grain boundaries. The selected-area electron diffraction (SAED) is conducted as shown in Figs. 4(c)–4(d) for the phase distribution. According to the SAED patterns, the LLZTO grain has an ordered diffraction spots corresponding to the $(\bar{2}00)$, (020), (220), and (200) crystal planes. The ordered crystal planes demonstrate a good crystallinity of the cubic lattice that confirms the XRD results. Figure 4(d) shows the electron diffraction patterns of (004) and (008) planes which are attributed to the grain boundary of weak crystallinity. Thus, we conclude that the sintered LLZTO pellets consist of crystallized grains in a network of amorphous grain boundaries. It is worth noting that the unidentified extra spots in addition to the (200) family in Fig. 4(d) may imply the new phases or defected structures at the grain boundaries. We also conduct energy dispersive x-ray analysis (EDX) to identify the elemental distribution in the sintered samples. Figure S2 in the supporting information demonstrates the uniform distributions of La, Zr, Ta and O in the LLZTO composites.

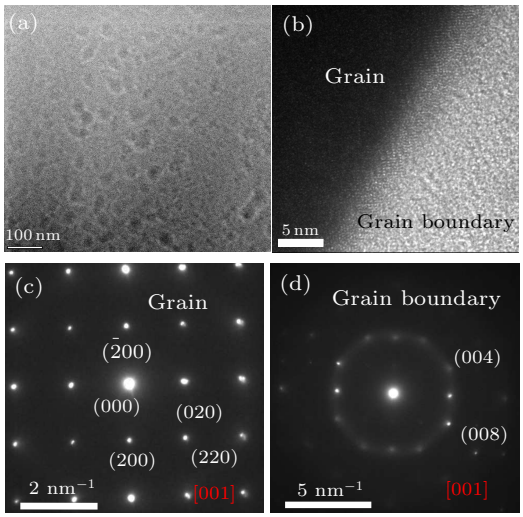


**Fig. 4.** (a) A TEM image of cross section of the LLZTO polycrystalline sample prepared by the focused ion beam. (b)–(d) The TEM micrograph, the SAED pattern of the grain, and the SAED pattern of the grain boundary, respectively.

To determine the mechanical properties in the LLZTO polycrystals of different densities, we perform grid nanoindentation to measure the elastic modulus $E$, hardness $H$, and fracture toughness $K_c$ to draw a correlation between the mechanical behavior and the sample porosity. Here the grid indentation is suited to measure the spatial distribution of the mechanical properties of samples of local heterogeneity. This technique relies on a large array of nanoindentation.

In our tests, we perform 5 × 5 grid indentations for each sample, and the spacing between the indents (30–50 μm) is much larger than the size of individual impression. Figure 5(a) shows the load-displacement curves of nanoindentation with the indentation depth of 2000 nm, and the inset shows the optical image of the impressions. No visible cracks exhibit around the grid impressions. Figure 5(b) displays a comparison of the elastic modulus (red squares) and hardness (blue squares) of the LLZTO composites of different relative densities. The mechanical properties vary drastically with the elastic modulus increasing from 105.49± 18.02 GPa to 158.47 ± 10.10 GPa and the hardness increasing from 3.72 ± 0.83 GPa to 11.27 ± 1.38 GPa, respectively, when the pellet density grows. The standard deviation derived from the 25 grid indents for all the sample is small. The condensed polycrystalline sample accompanied by the less porosity and defects and larger grains results in the increased elastic modulus and hardness which approaches to the intrinsic values of LLZTO. Figure 5(c) demonstrates the mechanical properties of LLZTO of 98% relative density at various indentation depths. In general, the maximum indentation depth should be chosen to avoid the effect of surface condition at shallow indentation and the substrate effect at deep indentation. Figure 5(c) shows the dependence of the elastic modulus and hardness on the indentation depth in the range of 600–2000 nm. Both properties are insensitive to the indentation depth with an average of 155.16 ± 2.12 GPa and 11.61 ± 0.55 GPa, respectively, which is consistent with the transgranular morphology of the sample with a minor porosity.

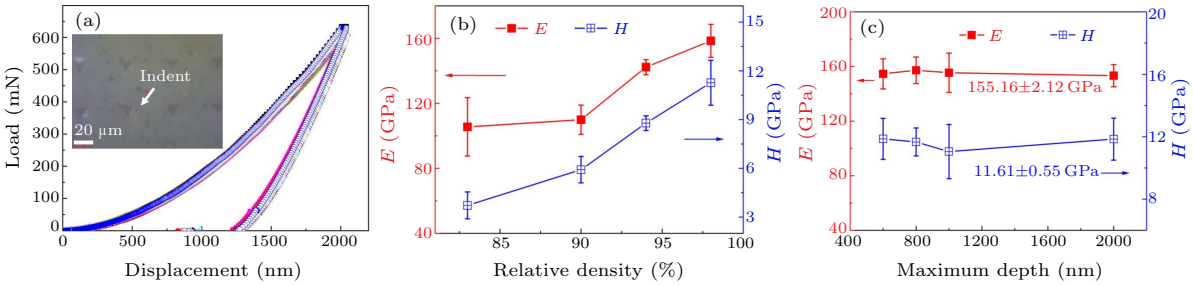


**Fig. 5.** (a) Load-displacement response of the LLZTO electrolyte upon nanoindentations. Inset shows an image of the matrix and the indents. (b) Elastic modulus (red line) and hardness (blue line) of the LLZTO pellets as a function of the relative density. (c) Dependence of elastic modulus (red line) and hardness (blue line) on the maximum indentation depth into the LLZTO pellet of 98% density.

Figure 6 further shows the SEM images of the grid impressions and the correlation between the mechanical response and the microstructural features of the LLZTO samples. Detailed spatial distributions of the mechanical properties of the pellets of different relative densities are compared. Figures 6(a) and 6(b) show the 5 × 5 grid indents in a polished LLZTO composite of 98% density at the indentation depth of 1500 nm. It is evident that the indentations are performed reliably at the targeted sites. The indentation depth is chosen appropriately, which does not induce mechanical damage around the impressions as shown in the enlarged surface area in Fig. 6(b). In comparison, Figs. 6(e) and 6(f) show the polished surface of the LLZTO composite of 94% density with a small fraction of the indents located near the pores. In the histogram plots of the spatial distribution of the mechanical properties in Figs. 6(c)–6(h), the elastic modulus and hardness of the LLZTO composites of 98% density are concentrated at the values of 160 GPa and 11 GPa, respectively, which is consistent with the plot in Fig. 5(c). It is noteworthy that the peak probability of the elastic modulus is as high as 0.42 with a narrow distribution in the range of 120–180 GPa, while the peak probability of the hardness is around 0.3 with a range of 8–14 GPa. The LLZTO composite of 94% density exhibits slightly smaller elastic modulus and hardness of 145 GPa and 9.0 GPa, respectively, with their probabilities being both around 0.33. Nevertheless, the histogram distribution shows a similar skewed feature. Overall, we conclude that the LLZTO pellets with the relative density over 94% possess good mechanical properties and minor defects and porosity.

We continue to assess the fracture property of the LLZTO polycrystalline pellets, and measure the fracture toughness $K_c$ of the sintered samples of different relative densities using the pop-in method in nanoindentation. A cube corner indenter is with a semi-apex angle of 35.3°. The sharp cube corner indenter facilitates initiation of radial cracks at lower load in brittle materials. $K_c$ is calculated using Eq. (4), and $\alpha$ is 0.036 as an empirical constant for the cube corner indenter.[36] Fracture toughness for the pellets of two different relative densities is shown in Fig. S3, where the crack length is directly obtained from the SEM images. However, it should be noted that the crack length is often difficult to measure by optical microscopy or electron microscopy in the small-volume materials. When radial cracks are generated by nanoindentation in the brittle samples, the load-

displacement curve exhibits a sharp increase in the indenter penetration. This sudden increase of the indenter displacement is referred as pop-in. Therefore, an effective crack length $c$ can be calculated by the equation,[5] which allows to estimate the crack length from the load-displacement curve rather than measuring $c$ under a microscope. In the equation,[5] $h_{\rm m}$ represents the penetration displacement of the indenter, $h_{\rm t}$ is the anticipated penetration in the hypothetical absence of the pop-in, and $h_x = h_{\rm m} - h_{\rm t}$.

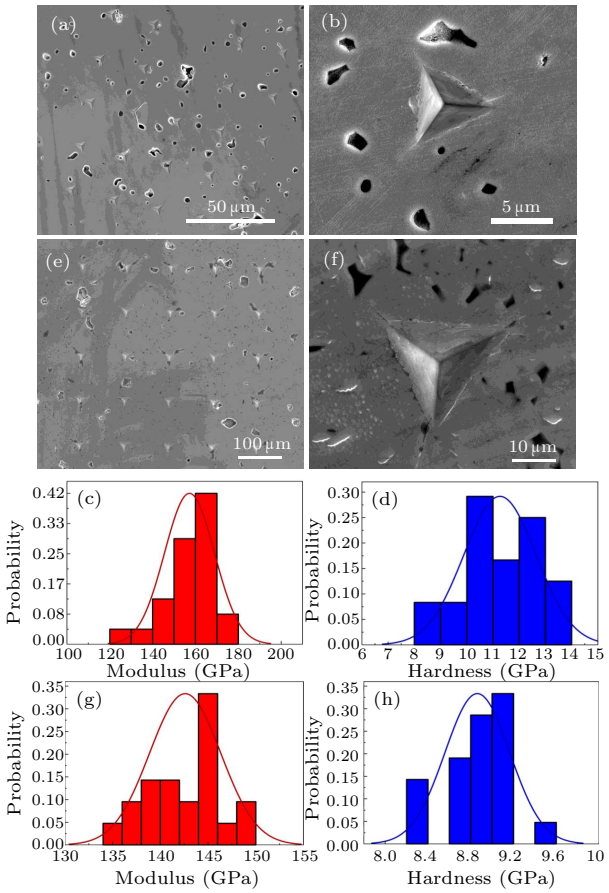


**Fig. 6.** SEM images of the grid indentation and impressions at 1500 nm indentation depth of the LLZTO pellets of different densities of 98% [(a), (b)] and 94% [(e), (f)]. Histogram distributions of elastic modulus and hardness of the LLZTO pellets of the densities of 98% [(c), (d)] and 94% [(g), (h)].

Figure 7 shows the results of the calculated fracture toughness of LLZTO composites of different relative densities. The red lines represent the load-displacement curves where the green portion following the pop-in events contains the data points used to calculate the fracture toughness. The black dashed lines are the theoretical load-displacement response without crack formation underneath the indenter. The crack length is calculated using the first eight points on the green lines. The results of $K_{\rm c}$ are represented by the blue solid circles. The fracture toughness of the LLZTO composites is determined to be 0.44, 0.81, and 1.51 MPa·m$^{1/2}$ for the sintered samples of the relative density of 83%, 94%, and 98%, respectively. The $K_{\rm c}$ values calculated from different data points are within a narrow range that verifies the robustness of the pop-in method. This is also due to the $Li_2CO_3$ additives that restrain the defect growth in the pellets. The fracture toughness reaches maximum for the LLZTO composite of 98% density. The fracture toughness of 0.44 MPa·m$^{1/2}$ for LLZTO of 83% density is found to be lower than the value of single crystalline LLZTO (∼0.7 MPa·m$^{1/2}$). This difference is attributed to the porosity in the polycrystalline sample where crack initiation and growth mostly follow an intergranular process.

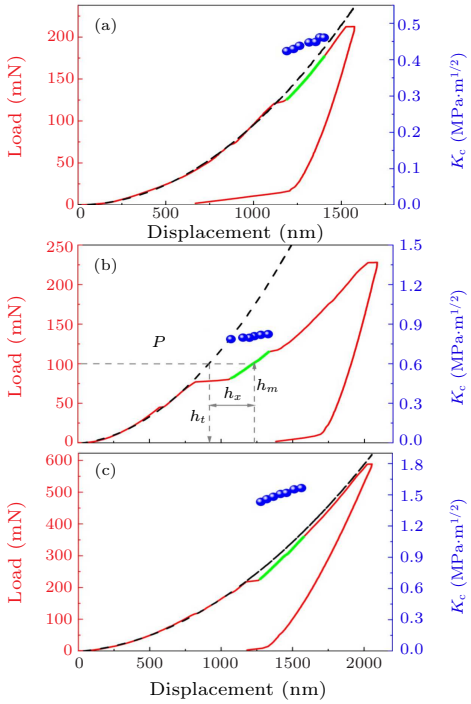


**Fig. 7.** Fracture toughness of the LLZTO pellets measured by the pop-in method. (a)–(c) The fracture toughness (blue dots) of the pellets with densities of 83%, 94%, and 98%, respectively. The green lines following the pop-in events contain the data points used to calculate the fracture toughness. We employ Eqs. (4) and (5) to determine the crack length and fracture toughness. The calculated crack length $c$ is validated by comparing with the experimental measurement using SEM.

As seen in Fig. S3b in the supporting information, the lower density LLZTO promotes the formation and propagation of radial cracks along the grain boundary. In comparison, the LLZTO composite of 94% density exhibits a much higher fracture toughness that is attributed to the larger grain size and lower porosity as shown in Fig. S3d. Cracks in the more compacted polycrystalline pellets are likely to propagate within the grains that follows a transgranular process and results in a higher fracture resistance. Another note is that the $K_{\rm c}$ values (0.44 and 0.81 MPa·m$^{1/2}$ for the sample density of 83% and 94%, respectively) are smaller than the fracture toughness measured using the SEM imaging-based

crack length (0.63 and 0.88 MPa·m$^{1/2}$, respectively). This is expected because the crack length determined by the scanning microscopy may be underestimated and embedded cracks in the bulk may not be observed on the sample surface. Compared to the literature results, the average $K_c$ for LLZTO of 98% density is in good agreement with the experimental results of Kim *et al.*,[37] which is in the range of 0.86–1.63 MPa·m$^{1/2}$. This value is slightly larger than other similar polycrystalline solid electrolytes, for instance, Wolfenstine *et al.* reported the fracture toughness of $Li_{6.19}Al_{0.27}La_3Zr_2O_{12}$ as 1.25 MPa· m$^{1/2}$,[38] and Schell *et al.* reported that the fracture toughness for $Li_{0.33}La_{0.57}TiO_3$ was 1.24 MPa·m$^{1/2}$.[39] Such a variation is within a reasonable experimental error given the complexity of the grain structures and a difference in the intergranular versus the transgranular behaviors for crack propagation.

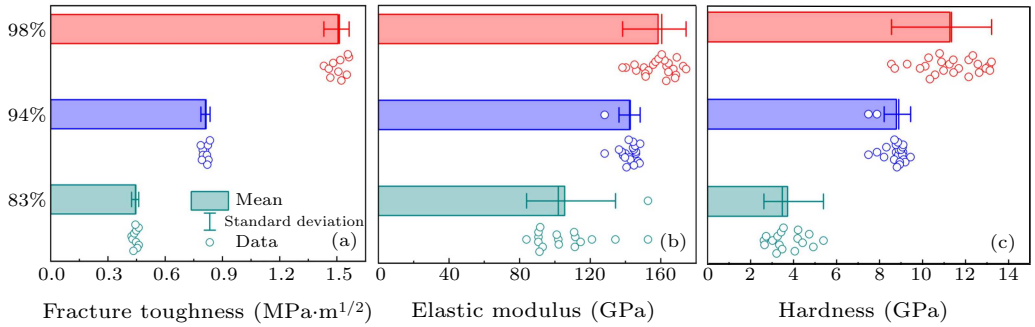


**Fig. 8.** Statistical representations of (a) fracture toughness, (b) elastic modulus, and (c) hardness of LLZTO pellets of different densities.

For a better view of the mechanical properties, Fig. 8 shows the fracture toughness, elastic modulus, and hardness of the sintered LLZTO pellets of different relative densities. The circles represent the individual indentation data point, the height of the bars represents the average values, and the error bars are the standard deviation. The general trend is that all the mechanical properties are largely enhanced when the pellet density increases. Starting from the sample density of 83%, the fracture toughness grows up to a factor of two for the 94%-density pellet and a factor of three for the sample density of 98%. Such a linear trend is due to the change of the grain boundary strength under different sintering conditions that fracture transits from the intergranular to the transgranular behaviors. Likewise, the elastic modulus and hardness for the porous sample of 83% density exhibit the lowest values, but the elastic and plastic properties for the samples in densities of 94% and 98% are close. The variation of the elastic modulus and hardness is largely dominated by the porosity and the grain size in the LLZTO composites. The grain size for all the sintered samples is over 2.79 μm and the impression size is typically less than 1 μm. Therefore, for the samples of larger grains, most of the indentation are located within the single LLZTO grains. For the LLZTO composite of 83% density, the average hardness is only 3.72 GPa because some indentations are located near the pores between the grains. Furthermore, the large standard deviation is also a result of the nonuniform grain interfaces and pore distribution. In comparison, for the pellet in density of 98%, the grain grows to the largest size of 13.21 ± 5.22 μm and most of grains are densified without visible grain boundaries. The measured elastic modulus and hardness are anticipated to approach the intrinsic values of LLZTO.

We perform the electrochemical impedance spectroscopy (EIS) measurement and the cyclic test to characterize the electrochemical performance of the sintered LLZTO solid electrolyte. The Pt coated LLZTO is used to conduct the impedance test. Figure 9(a) shows the Nyquist plots of the LLZTO composites. The resistance is attributed by the contributions from the bulk grains and the grain boundaries. The impedance profiles are composed of one quasi-semicircle at the high frequency and a straight line at the low frequency. The second intersection of the semicircle with the horizontal axis represents the overall impedance of the LLZTO electrolyte. The total conductivity $\sigma$ is determined using Eq. (1). The inset of Fig. 9(a) shows that the total impedance is around 1315 Ω, and the total conductivity $\sigma$ for the LLZTO composites of 98% density is $4.54 \times 10^{-4}$ S/cm. This value is very close to the high conductivity of $4.43 \times 10^{-4}$ S/cm in LLZTO prepared by oscillatory pressure sintering (OPS) reported by Li *et al.*[40] The ionic conductivity decreases drastically ($\sim 0.38 \times 10^{-4}$ S/cm) when the density of the pellets is reduced to 90%. The ionic conduction is highly dependent on the presence of the porosity in the polycrystals, which largely impacts the contact between the grains. To further evaluate the cycling stability of LLZTO composites, Fig. 9(b) shows the voltage profiles for the Li/LLZTO/Li symmetric cell using the 98%-density pellet and conducted with a current density of 0.05 mA/cm$^2$. The symmetric cell

maintains a stable Li striping/plating for over 100 cycles. More specifically, the inset shows the 1st–5th cycles and the 95th–100th cycles, which still exhibits a flat voltage profile indicating an excellent interfacial stability. These results demonstrate that the densified LLZTO composites are the major reason of the good cycling stability. The grain defects and porosity reduce the ionic conduction both in the bulk and across the interface, and thus deteriorate the electrochemical performance of the solid-state batteries.

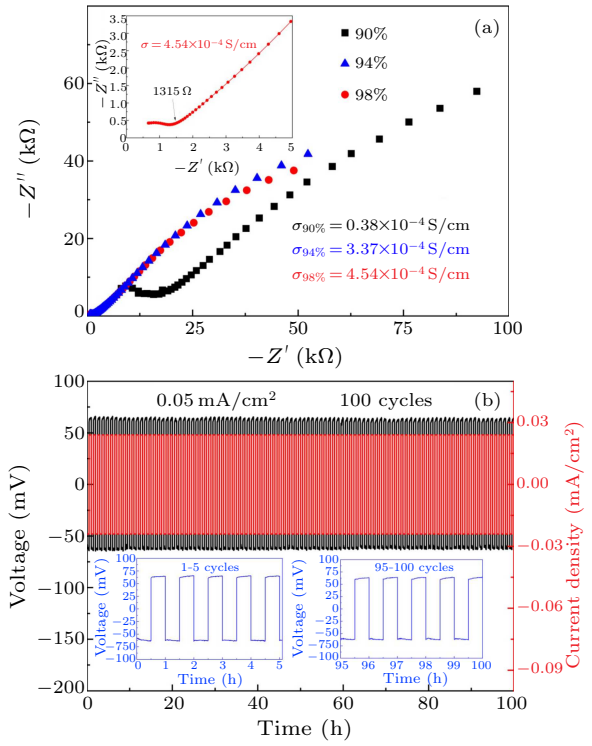


**Fig. 9.** (a) Nyquist plots of the LLZTO pellets of different densities. Inset shows the zoom-in view of the Nyquist plot for the sample density of 98%. (b) Cycling stability of the Li/LLZTO/Li symmetric cell at room temperature with a current density of 0.05 mA/cm$^2$ over 100 cycles. Insets are the voltage profiles for the 1st–5th cycles and the 95th–100th cycles.

In summary, we have synthesized LLZTO polycrystalline composites with different densities using the hot-pressing method. By controlling the excessive $Li_2CO_3$ additives, the compacted LLZTO pellets of the optimized mechanical properties are obtained. The grain size grows up to $13.21 \pm 5.22$ μm and the grain structure shows a transgranular feature in the pellet of 98% density. The elastic modulus and hardness increase monotonically with the increasing sintered sample density, and reach $158.47 \pm 10.10$ GPa and $11.27 \pm 1.38$ GPa, respectively, for LLZTO of 98% density. The enhanced mechanical properties are attributed to the reduced grain defects, lower porosity, and increased grain boundary strength in the compacted pellet. The fracture toughness is determined by the pop-in method using nanoindentation and the calculated crack length is compared with the one obtained by SEM images. The fracture toughness increases from 0.44 to 1.51 MPa·m$^{1/2}$, showing a transition from the intergranular to transgranular fracture behavior as the pellet density increases. The ionic conductivity reaches $4.54 \times 10^{-4}$ S/cm in the LLZTO electrolyte of 98% density, which is over ten times larger than that in the sample of 83% density. The stable cyclic voltage profile using the densified LLZTO pellet shows that the symmetric cell maintains a good Li striping/plating for over 100 cycles. This work presents systematic characterization of the mechanical properties of the LLZTO solid electrolyte, including the elastic modulus, hardness, and fracture toughness. The mechanical responses are rooted from the microstructural feature of the sintered polycrystals and have a strong impact on the electrochemical performance of the solid-state batteries.

## References


[1] Dunn B, Kamath H and Tarascon J M 2011 *Science* **334** 928
[2] Cheng F, Liang J, Tao Z and Chen J 2011 *Adv. Mater.* **23** 1695
[3] Qian J, Henderson W A, Xu W, Bhattacharya P *et al.* 2015 *Nat. Commun.* **6** 6362
[4] Pervez S A, Cambaz M A, Thangadurai V and Fichtner M 2019 *ACS Appl. Mater. Interfaces* **11** 22029
[5] Famprikis T, Canepa P, Dawson J A, Islam M S *et al.* 2019 *Nat. Mater.* **18** 1278
[6] Zheng F, Kotobuki M, Song S, Lai M O *et al.* 2018 *J. Power Sources* **389** 198
[7] Wang C, Ping W, Bai Q, Cui H *et al.* 2020 *Science* **368** 521
[8] Li S, Zhang S Q, Shen L, Liu Q *et al.* 2020 *Adv. Sci.* **7** 1903088
[9] Hu S, Chen W, Zhou J, Yin F *et al.* 2014 *J. Mater. Chem. A* **2** 7862
[10] Hu S, Yin F, Uchaker E, Zhang M *et al.* 2014 *J. Phys. Chem. C* **118** 24890
[11] Hu S, Chen W, Uchaker E, Zhou J *et al.* 2015 *Chem. Eur. J.* **21** 18248
[12] Tang Y, Zhang L, Chen J, Sun H *et al.* 2021 *Energy Environ. Sci.* **14** 602
[13] Zhong Y, Xie Y, Hwang S, Wang Q *et al.* 2020 *Angew. Chem. Int. Ed.* **59** 14003
[14] Golozar M, Paolella A, Demers H, Savoie S *et al.* 2020 *Sci. Rep.* **10** 18410
[15] Zhang X, Wang S, Xue C, Xin C *et al.* 2019 *Adv. Mater.* **31** 1806082
[16] Masias A, Felten N, Garcia-Mendez R, Wolfenstine J *et al.* 2019 *J. Mater. Sci.* **54** 2585
[17] Manalastas J W, Rikarte J, Chater R J, Brugge R *et al.* 2019 *J. Power Sources* **412** 287
[18] Kawahara K, Ishikawa R, Nakayama K, Higashi T *et al.* 2019 *J. Power Sources* **441** 227187
[19] Gao K, He M, Li Y, Zhang Y *et al.* 2019 *J. Alloys Compd.* **791** 923
[20] Shen F, Dixit M B, Xiao X and Hatzell K B 2018 *ACS Energy Lett.* **3** 1056
[21] Han F, Zhu Y, He X, Mo Y *et al.* 2016 *Adv. Energy Mater.* **6** 1501590
[22] Cheng E J, Sharafi A and Sakamoto J 2017 *Electrochim. Acta* **223** 85
[23] Kim S, Jung C, Kim H, Thomas-Alyea K E *et al.* 2020 *Adv. Energy Mater.* **10** 1903993
[24] Valle J M and Sakamoto J 2020 *Solid State Ionics* **345**

115170
[25] Matios E, Wang H, Wang C, Hu X *et al.* 2019 *ACS Appl. Mater. Interfaces* **11** 5064
[26] Zekoll S, Marriner-Edwards C, Hekselman A O, Kasemchainan J *et al.* 2018 *Energy Environ. Sci.* **11** 185
[27] Han G, Kinzer B, Garcia-Mendez R, Choe H *et al.* 2020 *J. Eur. Ceram. Soc.* **40** 1999
[28] Hong Y S, Li N, Chen H, Wang P *et al.* 2018 *Energy Storage Mater.* **11** 118
[29] Cho Y H, Wolfenstine J, Rangasamy E, Kim H *et al.* 2012 *J. Mater. Sci.* **47** 5970
[30] Xu R, Yang Y, Yin F, Liu P *et al.* 2019 *J. Mech. Phys. Solids* **129** 160
[31] De Vasconcelos L, Sharma N, Xu R and Zhao K 2019 *Exp. Mech.* **59** 337
[32] Ni J E, Case E D, Sakamoto J S, Rangasamy E *et al.* 2012 *J. Mater. Sci.* **47** 7978
[33] Yu S, Schmidt R D, Garcia-Mendez R, Herbert E *et al.* 2016 *Chem. Mater* **28** 197
[34] Sharafi A, Haslam C G, Kerns R D, Wolfenstine J *et al.* 2017 *J. Mater. Chem. A* **5** 21491
[35] De Vasconcelos L S, Xu R, Li J and Zhao K 2016 *Extreme Mech. Lett.* **9** 495
[36] Xu R, Sun H, de Vasconcelos L S and Zhao K 2017 *J. Electrochem. Soc.* **164** A3333
[37] Kim Y, Jo H, Allen J L, Choe H *et al.* 2016 *J. Am. Ceram. Soc.* **99** 1367
[38] Wolfenstine J, Allen J L, Sakamoto J, Siegel D J *et al.* 2018 *Ionics* **24** 1271
[39] Schell K G, Lemke F, Bucharsky E C, Hintennach A *et al.* 2017 *J. Mater. Sci.* **52** 2232
[40] Li H Y, Huang B, Huang Z and Wang C A 2019 *Ceram. Int.* **45** 18115

**Supplementary Material: Elastic modulus, hardness, and fracture toughness of $Li_{6.4}La_3Zr_{1.4}Ta_{0.6}O_{12}$ solid electrolyte**

Shan Hu,[1, 2] Pengyu Xu,[3] Luize Scalco de Vasconcelos,[2] Lia Stanciu,[3] Hongwei Ni[1,*], and Kejie Zhao[2,*]

[1]*State Key Laboratory of Refractories and Metallurgy, Wuhan University of Science and Technology, Wuhan 430081, China*

[2]*School of Mechanical Engineering, Purdue University, West Lafayette, Indiana 47907, USA*

[3]*School of Materials Engineering, Purdue University, West Lafayette, Indiana 47907, USA*

*Corresponding authors: nihongwei@wust.edu.cn (H. Ni), kjzhao@purdue.edu (K. Zhao).

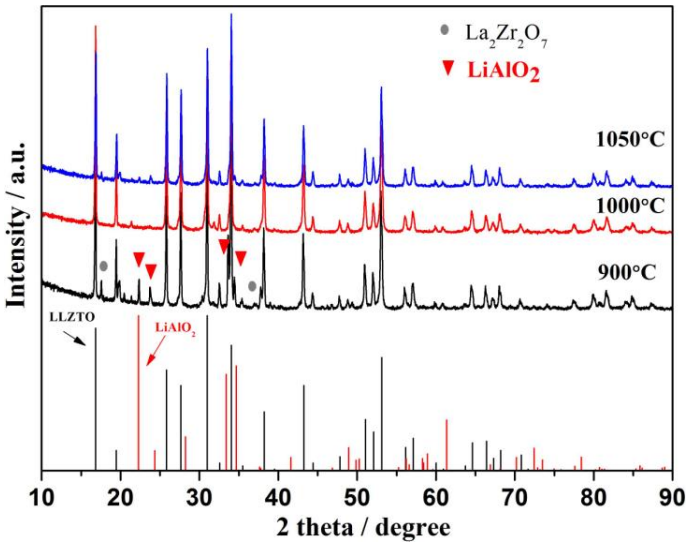


**FIG. S1**: XRD patterns of LLZTO composites synthesized at different annealing temperatures for 12h.

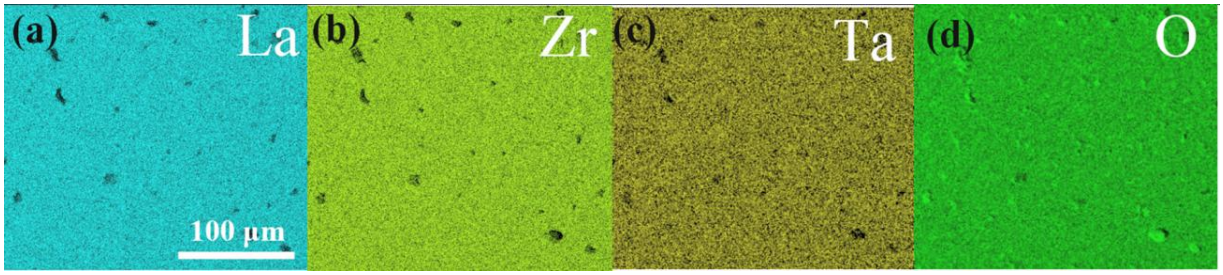


**FIG. S2**: The EDX mapping showing the elemental distributions of (a) La, (b) Zr, (c) Ta, and (d) O.

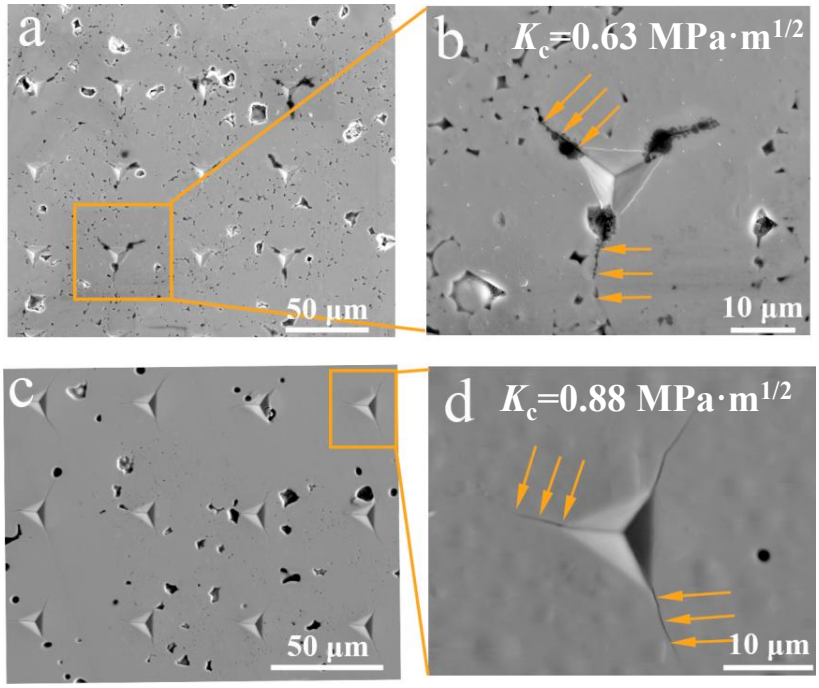


**FIG. S3**: Crack length determined by the SEM images. (a)-(b) show the indents and the crack length for LLZTO of the relative density of 83%, and (c)-(d) show the SEM images for the LLZTO sample of 94% density. The fracture toughness $K_c$ is calculated using the crack length determined by the SEM images, (b) $K_c$=0.63 MPa·m$^{1/2}$, and (d) $K_c$=0.88 0.63 MPa·m$^{1/2}$.